Energy Storage Materials 18 (2019) 269–279

Contents lists available at ScienceDirect

Energy Storage Materials

journal homepage: www.elsevier.com/locate/ensm

Superior electrochemical performance of sodium-ion full-cell using poplar wood derived hard carbon anode

Yuheng Zheng[a,b,c], Yaxiang Lu[a,*], Xingguo Qi[a], Yuesheng Wang[a], Linqin Mu[a], Yunming Li[a], Qiang Ma[a], Ju Li[b,c,d], Yong-Sheng Hu[a]

[a] Key Laboratory for Renewable Energy, Beijing Key Laboratory for New Energy Materials and Devices, Beijing National Laboratory for Condensed Matter Physics, Institute of Physics, Chinese Academy of Sciences, School of Physical Sciences, University of Chinese Academy of Sciences, Beijing 100190, China
[b] School of Materials Science and Engineering, Tongji University, Shanghai 201804, China
[c] Institute of New Energy for Vehicles, Tongji University, Shanghai 201804, China
[d] Department of Nuclear Science and Engineering and Department of Materials Science and Engineering, MIT, Cambridge, MA 02139, USA

ARTICLE INFO

Keywords:
Sodium-ion battery
Hard carbon
Wood
High-rate
Full-cell

ABSTRACT

As a supplement to lithium-ion batteries, the rate capability and cycling stability of sodium-ion batteries still need to be improved for practical applications. Here we report a novel poplar wood derived hard carbon anode, exhibiting a high specific capacity of 330 mAh/g and an initial Coulombic efficiency of 88.3% in half cells, and delivering a reversible specific energy of 212.9 Wh/kg (based on two-electrode masses) at 1 C and a long cycle life of 1200 cycles at 5 C when pairing with $Na[Cu_{1/9}Ni_{2/9}Fe_{1/3}Mn_{1/3}]O_2$ cathode in full cells. In addition, with the matched areal capacity of 2 mAh/cm^2 and under the industrial level cathode loading of 20.5 mg/cm^2, the capacity highly maintains at 2 C, and after 1400 cycles could almost fully recover by setting the current rate to C/10. This indicates sodium-ion batteries are approaching maturity.

1. Introduction

With graphite/LiC_6 anode, Sony successfully commercialized the first rechargeable lithium-ion battery (LIB) in 1991. Since then, massive efforts have been made to optimize the performance of LIBs in terms of both experiments [1] and modeling [2]. In this endeavor it is very important to maintain careful balance among individual material components (cathode, anode, electrolyte, separator, current collectors) in the full-cell. This includes (a) the areal capacity [mAh/cm^2] of cathode and anode should be roughly matched throughout a full-cell's life, (b) the liquid electrolyte (solvent and salt) should not be consumed too much relative to anode/cathode weight lest it dries out, (c) electrical percolation should be maintained inside cathode and anode coatings despite volume changes, (d) electrical insulation should be maintained across the separator despite thickness/temperature changes of the cathode and anode, (e) the binders and current collectors should not be corroded, (f) soluble species dissolved in the electrolyte (e.g. Mn cations from cathode) should not attack the solid electrolyte interphase (SEI) of the anode, (g) limited production of volatiles (gassing), etc. For these reasons, it can be misleading to over-optimize an individual metric like the gravimetric specific capacity [mAh/g] of an active material, while neglecting other crucial factors like the compressed pellet density, electrolyte/electrode ratio, and if the Coulombic Efficiency is above 99.5% or 99.9%. [3,4].

Lithium as an element resources are not only rare (17 ppm in Earth's crust), but also unevenly distributed, leading to speculations about “peak lithium” and future geopolitical instabilities. In particular, if grid-scale electricity storage is to be implemented as LIB *en masse*, Lithium resource could become limiting. In contrast, sodium is plentiful (23,000 ppm in Earth's crust). Currently, Na_2CO_3 is ~50× cheaper than Li_2CO_3. Furthermore, because Na is thermodynamically immiscible with Al, Al could be used as the current collector on both the anode and cathode side, simplifying cell fabrication and further decreasing the cost. And unlike Cu current collector which can be corroded at low full-cell voltage, there is no similar problem for Al, so the sodium-ion battery (SIB) full-cell can be discharged to 0 V, reducing safety concerns in storage and transportation. Despite these advantages, presently SIBs suffer from poor rate and short cycle life compared to LIB at the full-cell level.

In the last 10 years or so, a large variety of SIB cathode materials including oxides and polyanionic compounds [5–14] were developed. A bottleneck now shows up at the anode. Graphite could not host Na between its graphene layers [15,16]. Others like alloys [17–19], Ti-based oxides [20] and organic compounds [21,22] have been explored

* Corresponding author.
E-mail addresses: yxlu@iphy.ac.cn (Y. Lu), liju@mit.edu (J. Li), yshu@aphy.iphy.ac.cn (Y.-S. Hu).

https://doi.org/10.1016/j.ensm.2018.09.002
Received 16 May 2018; Received in revised form 2 August 2018; Accepted 5 September 2018
Available online 08 September 2018
2405-8297/

but suffer from either low tap/compressed density, high cost, or low initial Coulombic efficiency (ICE).

Scalable production of low-cost SIB anode materials with large capacity, high ICE and good rate performance are highly desirable. Amorphous carbons have been investigated as SIB anode due to relatively large interlayer distance, 0.37 – 0.41 nm typically, allowing Na hosting. Amorphous carbon can be classified into two types, soft carbons and hard carbons. For soft carbon, graphitization occurs above a high temperature of 2800 °C, but which is impossible for the latter [23]. Although soft carbon exhibits high capacity and good rate performance in LIBs, low ICE and specific capacities were usually observed in SIBs, except for anthracite derived soft carbon [24].

Hard carbon has also been intensively investigated as anode material in LIBs, especially for high power conditions, thanks to its good kinetic performance. A similar structure to soft carbon exists in hard carbon but is believed to be more porous, such as the "falling cards model" [25]. In recent few years, various forms of hard carbon were developed, especially from pyrolysis of natural biomass thanks to their renewable and environmentally-friendly character and low cost [26–31]. But the report for the application of hard carbon anode in sodium-matched full cell with high specific energy, good rate performance, and long cycle life is rare.

A high Coulombic efficiency in full-cell cycling is supposed to be essential for a long cycle life. There is a LIB industry lore that "a Coulombic efficiency of 99.9% is required for a full-cell to cycle 200 times", due to the calculation of

$$(0.999)^{200} = 0.8186, \quad (1)$$

as 80% capacity retention is a common criterion for energy storage device life. For prediction (1) to hold rigorously, the assumptions are that (A) we have a perfectly Li-matched anode and cathode initially, (B) The anode potential falls below the electrochemical stability window of the liquid electrolyte, and therefore solid-electrolyte interphase (SEI) layer will form on any exposed anode surface that conducts electrons, (C) The Coulombic inefficiency (CI), which is defined as 1-CE, reflects the imbalance of free electron flows in the outer circuit within a charge-discharge cycle, has a one-to-one correspondence with the imbalance of free Li^+ ion trade between cathode and anode, and is accommodated by the formation of SEI at the anode. And we know from post-mortem chemical analysis that the cycled anode indeed contains non-cyclable Li trapped as Li_2O, LiF, etc. The accumulation of Coulombic inefficiencies CI = 0.001 over 200 cycles would give a Coulombic inefficiency cumulant (CIC) of $0.001 \times 200 = 20\%$ if we ignore the "compound interest" effect, thus the CE = 0.999 → 200 cycles → 20% capacity loss connection in prediction (1). The idea here is that with a "bad partner" in the full-cell - the anode - the initial cyclable Lithium inventory brought by the cathode will be gradually converted to non-cyclable Lithium trapped in SEI coating and SEI debris near the anode, and the full-cell will die out of "Lithium exhaustion".

While the above-mentioned process is certainly happening, whether the Coulombic inefficiency cumulant (CIC) analysis suggested by (1) truly holds quantitatively needs to be checked. Assumption (C), for example, states that the only redox-active species that traverses the liquid electrolyte in a non-blocking manner are free Li^+ ions. However, it has been shown [32,4,3] that other soluble redox-active species can also exist in the electrolyte, in which case (1) will not work precisely. For newer full-cell architectures like sodium-ion batteries, it behooves us to check to what degree CIC prediction works in predicting full-cell capacity decay. If assumptions (A), (B), (C) are tenable, the actual full-cell capacity decay should be *worse* than the CIC prediction, since there are other parallel mechanisms of battery degradation (listed in the first paragraph) besides lithium/sodium exhaustion. On the other hand, if the actual full-cell performance turns out to be *better* than the CIC prediction, then it indicates the presence of soluble redox mediators (SRM) in the electrolyte. [32,4,3].

Here we report a SIB architecture that is cost- and performance-competitive against LIB, which involves $Na[Cu_{1/9}Ni_{2/9}Fe_{1/3}Mn_{1/3}]O_2$ (NCNFM) [12] as cathode material and a newly developed low-cost biomass-derived hard carbon as anode material. This hard carbon is produced from one step pyrolysis at 1400 °C of poplar wood (PHC1400), and thanks to its specific capacity of ~330 mAh/g and the ICE of 88.3%, the CR2032 full-cells delivers a reversible specific energy of 212.9 Wh/kg at 1 C, and 165.8 Wh/kg at 5 C with a long cycle life of 1200 cycles. Significant SRM effect is found in the cycled electrolyte, which induces enormous *reversible* Coulombic inefficiency and breaks the prediction of (1). When applied with a cathode mass loading of 20.5 mg/cm^2 (~2 mAh/cm^2), which meets the demand of industrial application, the coin cell shows outstanding specific energy and only a capacity fading of about 6% after cycling for 600 cycles at a charging and discharging rates of 2 C. Importantly, the capacity could recover nearly completely after 1400 cycles by setting the current rate to C/10, which implies the active material barely degraded, and the anode and cathode materials are both nearly mature for SIBs.

2. Material and methods

2.1. Materials synthesis

Hard carbon was prepared by pyrolysis of poplar wood in one step. The poplar wood was collected in Hebei province, China. Typically, 3 g of xylem of the sample was smashed and carbonized for 2 h in a tube furnace under Argon flow. The pyrolysis temperatures were 1000 °C, 1200 °C, 1400 °C and 1600 °C, respectively, and then the samples were labeled as PHC1000, PHC1200, PHC1400, PHC1600.

2.2. Material characterization

The structure was characterized by an X'Pert Pro MPD X-ray diffractometer (XRD) (Philips, Netherlands) using Cu – Kα radiation (1.5405 Å) and Raman spectra (JY-HR 800). The morphologies of the samples were investigated with scanning electron microscope (SEM) (Hitachi S-4800). Transmission electron microscope (TEM) pictures were taken on a FEI Tecnai F20 TEM. BET isotherms were determined by nitrogen physisorption on a Micromeritics ASAP 2020 analyzer.

2.3. Electrochemical test

All electrochemical tests were conducted in CR2032 coin cells.

PHC sample was mixed with sodium alginate with a mass ratio of 95:5, then deionized water was added to make slurry, which was subsequently coated on Al foil, to serve as anode for both half-cell and full-cell tests. The as-prepared electrodes were dried at 120 °C in vacuum for 6 h. Commercial electrolyte from SHANGYANG Corp., a solution of 1 M $NaPF_6$ in ethylene carbonate (EC) and dimethyl carbonate (DMC) (1:1 in volume), with additives to stabilize the SEI formation and to improve the high voltage performance was utilized. Glass fiber was used as the separator.

For the half-cells, sodium metal foil was used as the counter electrode. Full-cells was constructed with PHC1400 as the anode material and $Na[Cu_{1/9}Ni_{2/9}Fe_{1/3}Mn_{1/3}]O_2$ as cathode. We measure a sequence of electrical charges [mAh] flowing through the outer circuit:

$$Q_C(1),\ Q_D(1),\ Q_C(2),\ Q_D(2),\ \ldots\ Q_C(n),\ Q_D(n),\ \ldots > 0 \quad (2)$$

material in a CR2032 cell. Synthesis method of the NCNFM material was a conventional solid state reaction [12]. The procedure of making cathode was same as the anode, except for the slurry compositions, which were 7:2:1 for the weight of the active material, super P and PVDF for the ordinary-loading cathode, and 93:3.5:3.5 for the high-loading cathode. The loading mass of the PHC was around 2.0 mg/cm^2 for the ordinary-loading anode and 7.0 mg/cm^2 for the high-loading anode. The capacity of the anode was designed to be 3%–5% beyond

the capacity of the cathode to avoid sodium metal deposition. All the cell assembly operations were performed in an Argon-filled glove box. The half-cells were cycled in a voltage range between 0-2.5 V. The full cells were cycled in a voltage range of 1.5-4.0 V at a current rate of C/10, 1C, 2C and 5C, and a voltage range of 0-4.0 V at a current rate of 1 C.

The discharge and charge tests were carried out on a Land BT2000 battery test system (Wuhan, China) at room temperature.

The cyclic voltammetry (CV) and electrochemical impedance spectra (EIS) are performed with an electrochemical workstation (CHI650D, Shanghai Chenhua Instrument Co., Ltd., China). For EIS, the amplitude of the ac signal was kept at 5 mV, and the frequency range of measurement was 1000 KHz to 0.05 Hz. Impedance data were analyzed by using the electrochemical impedance software Zview (version 3.5d, Scribner Associates Inc.).

3. Results and discussion

We first demonstrate the full-cell performance using the newly derived PHC material, which is very cheap and based on a renewable resource. The cathode-active (CA) material is NCNFM (the XRD pattern of NCNFM is provided as Supplementary Fig. S1), with half-cell specific capacity of 118 mAh/g (2.5-4.0 V). The anode-active (AA) material is PHC1400, with half-cell specific capacity of 330 mAh/g (0-2.5 V). Based on their specific capacity, the mass-loadings for the CA and AA are around 6.0 mg/cm^2 and 2.0 mg/cm^2 respectively, in roughly 3: 1 ratio. The exact loadings of the CA and AA in a full cell are carefully matched with their capacities, with an excess capacity of 3%–5% for AA, to prevent over-sodiation of the hard carbon anode. However, part of the Na^+ from cathode would be trapped when SEI is formed on anode in the first cycle, and the reversible full-cell capacity is found to be 101.1 mAh/g(CA) (85.6% of the reversible specific capacity of the cathode in half-cells). In later cycles, we have carefully tracked the capacity loss using the "Coulombic inefficiency cumulant" (CIC) and the "capacity fade ratio" (QF) analysis [4]. Then we evaluated the SRM effect with the 'reversible Coulombic inefficiency cumulant' (RCIC). The result of these full-cell tests are reported firstly. We will see excellent full-cell cycling performance to more than 1000 cycles, with a charging and discharging rate up to 5 C.

However, the areal capacity of the full-cell above is still low, only about 0.6 mAh/cm^2, which is far less than the industrial level (~2 *to* 5 mAh/cm^2 in commercial LIBs). Then we more than tripled the loading on both sides, with PHC1400 loading on the anode side reaching ~7 mg/cm^2, and the NCNFM loading on the cathode reaching 20.5 mg/cm^2. The areal capacity is now ~2 mAh/cm^2, which is of industrial relevance. Surprisingly, this full-cell still performed very well at 2 C with nearly no decay in capacity after 600 cycles. Further more, after cycling the cell for 1400 times at 2 C, the capacity could recover nearly completely when setting the current rate back to C/10, which implies the active materials barely degraded. This kind of performance is very encouraging. In fact, we limit the areal capacity at 2 mAh/cm^2 not because of capacity fading, but on account of too much polarization, and we expect an even more attractive performance of this architecture in the pouch cell.

We then give detailed explanation of the PHC properties. Among the samples, PHC derived at 1400 °C (PHC1400) exhibits the highest capacity (330 mAh/g) and ICE (88.3%). BET surface areas from the N_2 adsorption/desorption experiment were commonly provided in previous works to roughly evaluate the amount of SEI formed on the surface of anode in the first cycle. Interestingly, we found that BET surface area increased ~20 times when the pyrolysis temperature increased from 1400 °C to 1600 °C (PHC1400 vs. PHC1600). However $ICE_{PHC1600}$ is just slightly lower than $ICE_{PHC1400}$, which indicates that the additional surface area, which is mainly contributed by the pores with a typical width around 1 nm, is apparently not covered by SEIs. This is perhaps unsurprising in hindsight since the minimum reported SEI thickness is about 1 nm, and the electrolyte solvent and the anion may find it difficult to diffuse into and wet these 1 nm pores. Thus, BET surface area is not always appropriate for quantifying the real electrochemical active area and the SEI forming ability of the anode materials.

Hard carbons are usually marked with poor rate performances in SIBs, so much effort has been made to dope N, S or P into the hard carbons, to get relatively 'better' rate performance in half cells [33–41]. We also got huge capacity fading of the half-cells at high current densities. But, noting the rate performance of full-cells demonstrated in the "Full-cell performance" section 3.1, there must be an underestimation of the rate performance of hard carbon in half-cells. The capacity of half-cell is then proved to be more sensitive to polarization than that of the full-cell, and the half-cell encounters more polarization, which intensifies the underestimation of the real capacity of hard carbon anode. The apparant "poor rate performance" of the hard carbon anode in half-cell tests can actually be a measurement artifact. Thus, plain hard carbon could serve as the high rate anode material in SIBs, thanks to its much higher ICE than the N, S or P-doped samples.

3.1. Full-cell performance

Full-cells were assembled using PHC1400 anode and NCNFM cathode, then cycled at rates of C/10, 1 C, 2 C and 5 C, within full-cell voltage window $[U_{min}, U_{max}] = [1.5\ V, 4\ V]$. We measure a sequence of electrical charges [mAh] flowing through the outer circuit $Q_C(1)$, $Q_D(1)$, $Q_C(2)$, $Q_D(2)\ldots$, $Q_C(n)$, $Q_D(n)\ldots$, and from this sequence we get (see the Supplementary) CE(n)(Coulombic efficiency), CI(n)(Coulombic inefficiency), ICE(initial Coulombic efficiency), CIC(n)(Coulombic inefficiency cumulant), QR(n)(capacity retention ratio), QF(n)(capacity fade ratio).

It shows algebraically that if

$$Q_C(n+1) = Q_D(n) \tag{3}$$

for all n, then

$$\mathrm{QF}(n) = \mathrm{CIC}(n). \tag{4}$$

In other words, the Coulombic inefficiency cumulant would be the perfect predictor of capacity fade. But if on the hand

$$\mathrm{QF}(n) < \mathrm{CIC}(n) \tag{5}$$

which means the capacity fade turns out to be more *optimistic* than the CIC prediction, then there has to be

$$Q_C(n+1) > Q_D(n) \tag{6}$$

for some n. This can be somewhat counter-intuitive (if we believe the electrolyte only transmits Na^+ in a non-blocking manner), since it would mean the number of Na^+ that comes out of cathode in $n+1$ would exceed the number of Na^+ that was returned to it in n; this would not be a problem if the cathode has some reserves, but as we assumed in Supplementary equation (S5), there should be no intentional reserves. As we shall see later, (5) can be attributed to the presence of SRM in the electrolyte, once electrolyte-anode reactions are occurring.

Table 1[1] and Fig. 1a-d present full-cell performance at different C-rates. Except for the ICE data, all the other data in Table 1 were taken from the 10th cycle, when the Coulombic efficiencies were beyond 99.5%. At C/10 (Fig. 1a), the full-cell specific capacity $q(n = 10)$ is 79.8 mAh/g ($q^{NCNFM}(n = 10)$=101.1 mAh/g), with an ICE of 75.1%. The full-cell energy density $d(n = 10)$ is 225.5 Wh/kg. The definitions of these quantities are given in the Appendix.

As shown in Table 1, the performance of the full cell at 1 C is similar to the C/10 condition, with only a specific energy reduction of 5.6%.

[1] Note that we use $q(n = 10)$ to characterize the full-cell performance in this table, since it is easy to compare with other works; but we also use q^{NCNFM} in other conditions, thanks to its facility to compare with the Material Capacity(NCNFM).

Table 1
Full-cell performance, characterized by the initial Coulombic efficiency, full-cell specific capacity q (in discharge), energy density d (in discharge) and round-trip energy efficiency η. The definitions of these quantities are given in the Appendix.

Rate	ICE	$q(n = 10)$[mAh/g]	$d(n = 10)$ [Wh/kg]	$\eta(n = 10)$
C/10	75.1%	79.8	225.5	94.6%
1 C	83.2%	70.0	212.9	94.5%
2 C	82.5%	64.5	193.9	91.1%
5 C	79.4%	58.3	165.8	83.4%

Increased polarization could be observed at 5 C (Fig. 1b) compared to C/10, but the specific capacity still retained 58.3 mAh/g as Table 1 shows, corresponding to 165.8 Wh/kg. Along with the cycling times n as Fig. 1b presented, the discharging voltage decays and charging voltage rises continuously, which implies a gradual rise in impedance. The dQ/dV curve at 2nd cycle at C/10 is provided in Supplementary Fig. S2.

The utilization of aluminum as the negative current collector would reduce the cost of the cell, and also bring some safety improvement, as this enables the 0 V storage of the cell for SIBs. In a typical LIB cell, the copper current collector would be corroded by oxidation if the cell is over-discharged. Therefore LIBs must be transported and stored while holding charge, which is pretty dangerous. Our SIB does not have this problem: as shown in Fig. 1c and Supplementary Fig. S3, the full-cell was cycled between 0 V and 4 V, and after 400 cycles, 89.5% of the initial reversible capacity still remains.

Our full-cells demonstrate long cycle lives even at very high charging and discharging rates. Fig. 1d presents the long-term cycling performance at 5 C of the full-cell. About 71% of the initial reversible capacity remains after 1200 cycles. The long-term cycling at 5 C charging/discharging show a steady-state Coulombic efficiency through the 1200 cycles:

$$\mathrm{CE}_{\mathrm{steadystate}} \equiv \frac{1}{1200 - M} \sum_{n=M+1}^{1200} \mathrm{CE}(n) \tag{7}$$

of about 99.8% ($M = 1$), or

$$\mathrm{CI}_{\mathrm{steadystate}} \equiv 1 - \mathrm{CE}_{\mathrm{steadystate}} \approx 0.002. \tag{8}$$

This certainly conflicts with prediction (1), since a crude estimate would give $0.998^{1200} = 0.0905$, so the CIC would predict that only ~ 10% of the capacity should remain, since most of the cycleable Na is lost. Yet in reality, our full-cell still shows 71% of the initial reversible capacity at the 1200th cycle!

To analyze the capacity fading, CIC(n) and QF(n) are plotted together in Fig. 1e. After 1200 cycles, CIC(n) exceeds 150% but QF(n) is no more than 50% (including the inefficiency of 20.6% of the first cycle). So the CIC prediction is many times more pessimistic than the actual full-cell performance. Thus, $\mathrm{CI}_{\mathrm{steadystate}}$ cannot be only induced by the mechanism of Na^+ trapping in solid SEI as assumption (C) suggests, according to (5). The existence of SRM in SIBs is strongly suspected [3]. To confirm the existence of SRM, cycled cells were disassembled and the electrolyte was carefully absorbed with a fresh glass fiber separator. The separator with absorbed electrolyte was then assembled into a coin cell, without the original anode and the original cathode. Cyclic voltammetry experiments were then performed, simultaneously with a coin cell containing fresh

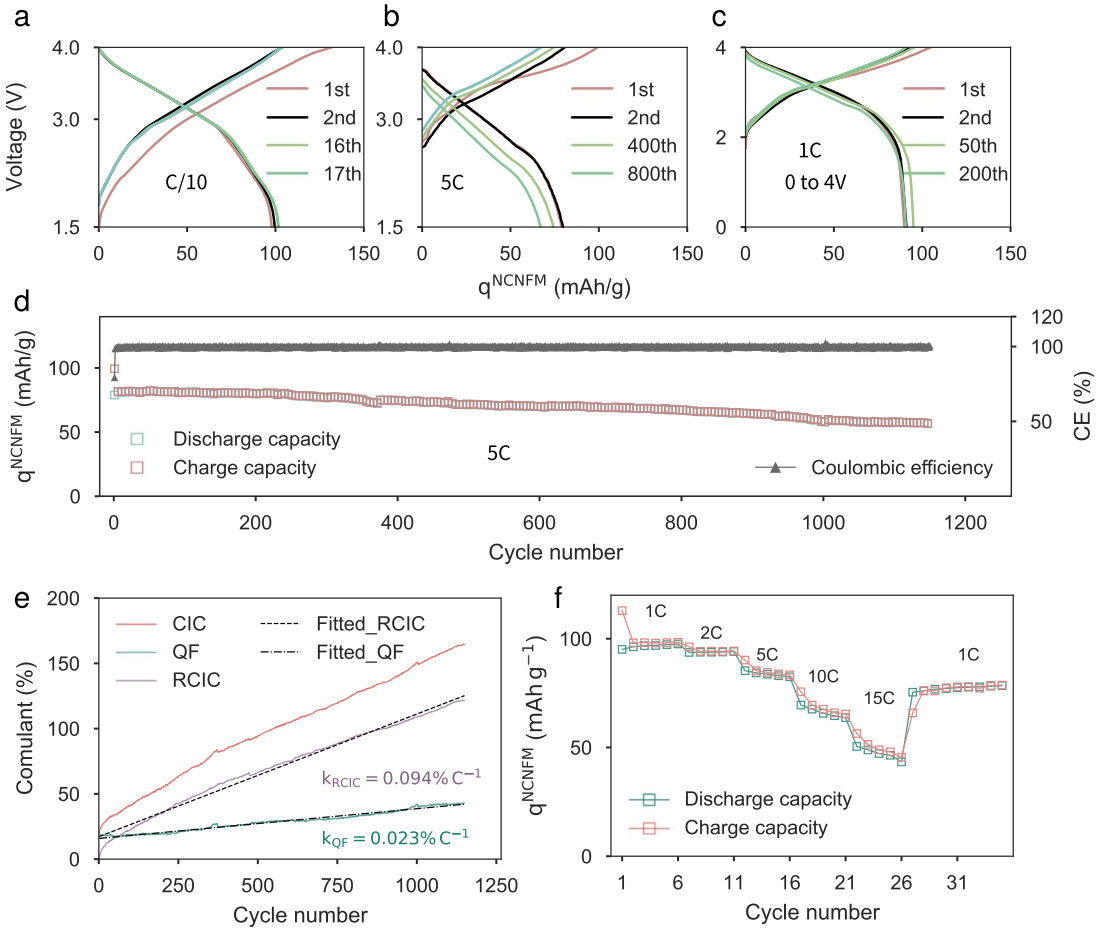

Fig. 1. Full-cell performance. Charge/Discharge profiles at the current rate of (a) C/10 and (b) 5 C between 1.5 and 4.0 V, (c) 1 C between 0 and 4.0 V. (d) The long-term cycling performance at 5 C, (e) Coulombic inefficiency analysis at 5 C, (f) the rate performance of the full-cell. The mass loadings were about 2 mg/cm^2 and 6 mg/cm^2 for the anode and cathode respectively. Specific capacities are provide from the cathode side.

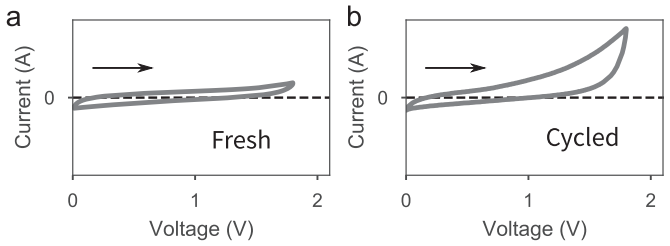

Fig. 2. The CV evidence of the existence of SRM. The second cycle of the CV curves of the coin cell contains only electrolyte wetted glass fiber separators, with (a) fresh electrolyte and (b) full-cell cycled electrolyte. The voltage window was set to 0–1.8 V (against Fe/Fe^{2+}), corresponding to 2.27–4.07 V against Na/Na^+, and the scan rate is 5×10^{-4} V/s.

electrolyte as a comparison. The voltage window is set to 0–1.8 V, and noting that the relative potential of Fe/Fe^{2+} (the cell wall) vs. Na/Na^+ is about 2.27 V, then this voltage window corresponds 2.27–4.07 V against Na/Na^+. The result is shown in Fig. 2. The fresh electrolyte exhibits a capacitor-like CV curve shown in Fig. 2a, in which the current integration is roughly zero in the cycle. But there exists a significant net imbalance of current flow for the cycled electrolyte, as presented in Fig. 2b, which means there must be soluble species in the liquid electrolyte that can participate in Faradaic processes. These soluble species seems to be oxidizable - we speculate they are generated near the original anode as SRM^{x-}, when U is large in the full-cell and $\dot{U} \equiv dU/dt$ is negative. SRM^{x-} will waft through the liquid electrode and lose electrons to the cathode, and return as SRM that is still soluble by concentration-driven diffusion. This way, the electrolyte will be effectively transporting $Q_{leak}(n)$ electrons from anode side to cathode side in a non-blocking manner, during the cycling of the full-cell:

$$\underbrace{Q_D(n) + Q_{leak}(n)}_{\#electrons} = \underbrace{Q_{D,Na^+}(n)}_{\#Na^+} \tag{9}$$

and

$$\underbrace{Q_C(n+1) - Q_{leak}(n+1)}_{\#electrons} = \underbrace{Q_{C,Na^+}(n+1)}_{\#Na^+} \tag{10}$$

(the sign convention is we try to make all the Q's positive), and assuming that Na^+ is completely reversible during cycling ($Q_{D,Na^+}(n) = Q_{C,Na^+}(n+1)$), there would be

$$Q_C(n+1) > Q_D(n). \tag{11}$$

In other words, the number of electrons metered through the outer circuit is actually less than the number of cycleable Na^+ traverses the electrolyte in discharge, and more than that in charge. This "leakage of electrons" *inside* the battery resolves the "cathode-side paradox" stated at (6). It has similar origin to the self-discharging phenomenon in charged batteries, with verified open external circuit.

We can define the "reversible Coulombic inefficiency cumulant" (RCIC):

$$\mathrm{RCIC}(n) \equiv \mathrm{CIC}(n) - \mathrm{QF}(n) \tag{12}$$

which is an indicator for this effect. In the demonstration presented in Fig. 1d, the slope of fitted RCIC is more than 4 times larger than that of the fitted QF. This means the actual capacity retention of our sodium-matched NCNFM//PHC full-cell is >5× more optimistic than naive CIC predictions like Eq. (1)! This is an enormous effect for SIB, and empirically much more distinct from the traditional graphite-based Li-ion battery and even Si-anode Li-ion battery (see e.g. Fig. 6d of [4]):

$$\left.\frac{\mathrm{RCIC}(n)}{\mathrm{CIC}(n)}\right|_{our\ SIB} > \left.\frac{\mathrm{RCIC}(n)}{\mathrm{CIC}(n)}\right|_{common\ LIBs} \tag{13}$$

With such a strong SRM effect, the full-cell performance would be more optimistic than the CIC prediction. Note there will be some extra energy loss through the SRM^{x-}/SRM shuttling, but from a practical point of view, a $CI_{steadystate} = 0.2\%$ (which combines the reversible SRM and the irreversible inefficiencies) gives negligible contribution compared to the polarization loss in the total energy inefficiency $1 - \eta(n)$, which is on the order of 5 to 10% per cycle as Table 1 shows.

With SRM^{x-}/SRM, there is a possibility of enhanced self-discharge also, in the following common use scenario of SIB: charge-hold-discharge, instead of immediately discharging after charging. To check whether this is a big problem, we have performed hold time t_{hold}-dependent voltage measurements of our SIBs (our previous data are all with $t_{hold} = 0$). We charge the full-cell to about 3.7 V, and then hold the voltage constant for 1 h to achieve a thermodynamically stable state, then hold the current 0 mA with $t_{hold} = 1$day, $t_{hold} = 3$days and $t_{hold} = 10$ days. Supplementary Fig. S4 shows the self-discharging profiles and the reproducibility is pretty good. One could find a SRM^{x-} consuming region at the first day, a SRM^{x-} exhausting region in the 2nd and 3rd day, and a following linear self-discharging region, with a rough rate of 0.004 V/day. It is seen that the self-discharge rate is still completely acceptable for most applications, even for grid-scale storage. The reason for this, despite the enhanced SRM^{x-}/SRM activity, is that the SRM^{x-} are likely generated only when the voltage is changing and the anode SEI is actively evolving, and could be consumed nearly completely in 1 day. In other words, during hold, the SRM^{x-} concentration (a function of both U and $\dot{U}$, not just U) is very low after 3 days, and therefore the static-hold energy leakage rate is very low.

As the capacity retains about 73% of low-rate specific capacity at 5 C, rate performance was performed to examine the rate capability of the full-cell. As Fig. 1f presents, even at a high current rate of 15 C, the full-cell delivers about q^{NCNFM}=50 mAh/g, about 50% of the C/10 condition. But the capacity fades quickly in the high rates of 10 C and 15 C, and this could be caused by the reaction between the electrolyte and the freshly deposited sodium metal on the electrode surface at high current rates.

3.2. High loading full-cell performance

As excellent performance of the full-cell at low loading (~0.6 mAh/cm^2) was achieved in the laboratory, it would be valuable if our system could work with industrial-level loadings. Positive electrode with a mass loading of 20.5 mg/cm^2 (the active mass ratio is 93%) was fabricated, and then applied in coin cells along with the PHC1400 anode (~7 mg/cm^2 with an active mass ratio of 95%). The results are shown in Fig. 3.

Compared to the coin cell with a matching areal capacity of 0.6 mAh/cm^2, q^{NCNFM} only decreased to about 80 mAh/g from 89.9 mAh/g at 2 C, when the matching areal capacity reached ~2 mAh/cm^2, indicating slight increase of polarization caused by longer diffusion paths of the Na^+ in the electrolyte. At 3 C, although the capacity fades to about 50% of the capacity at 2 C, it still cycled stably, according to Supplementary Fig. S5. This implies 3 C is still acceptable for the anode, and no Na metal deposition occurred on the anode side. For applications, there could be more flexible charging strategies, and 3 C could be part of one specific strategy. And further more, cycling stably means that there is no Na metal deposition all over the whole anode, and considering the irregular current density in smaller CR2032 cell, there must be some part on the anode where the current density breaks this limit.

The possible modes of Na metal deposition on the negative current collector were observed in the 2C condition, when the 8 × 8 mm^2 square-shaped anode and cathode were applied (Supplementary Fig. S6). Interestingly, if we make the negative electrode in round shape, and slightly larger in area than the positive electrode, sodium deposition effect could be avoided, and the cycling performance was improved significantly, as shown in Supplementary Fig. S7 and Fig. 3d. Compared with the capacity fading at 1 C (Supplementary Fig. S7), the anode-larger full-cell exhibited ultra stable cycling even at 2 C. No capacity decay could be found in the first 400 cycles, and only a decay of 6% was observed at the 600th cycle. And it is known that in the pouch cell and 18,650 cell for industrial application, the negative

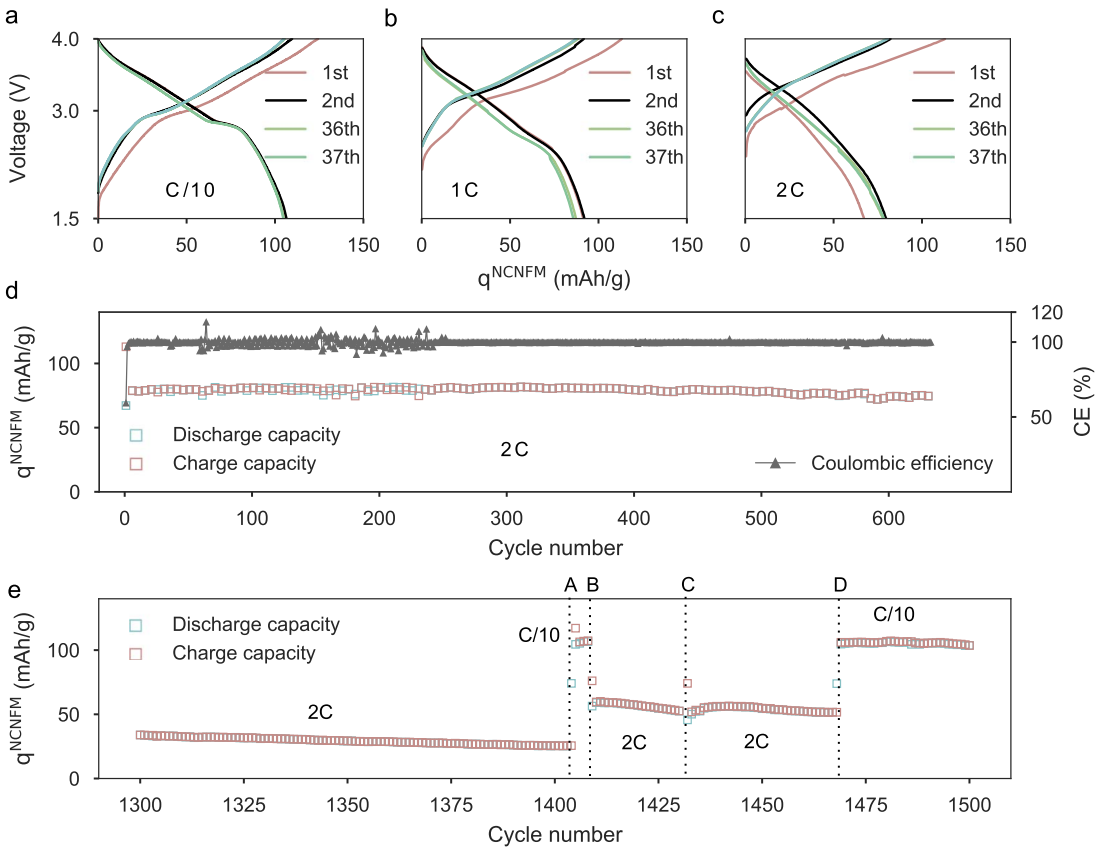

Fig. 3. The industrial level mass loading full-cell performance. Voltage profiles of (a) C/10, (b) 1C, (c) 2C, (d) Cycling performance of 2 C and (e) Primarily decay analyzing. Note that for the 2 C condition, the negative electrode was prepared in round shape and slightly larger in area than the positive electrode, to prevent the side deposition of Na metal on the negative current collector. The mass loading was about 7 mg/cm^2(ratio of the active material was 95%) and 20.5 mg/cm^2 (ratio of the active material was 93%) respectively for the anode and the cathode.

electrode is usually slightly larger than the positive electrode. Thus, we expect this system would work even more stably with industrial fabrication.

We also analyzed the mechanical degradation mechanism as shown in Fig. 3e. After 1400 cycles, we shook the full-cell by hand for 10 minutes, and then set the current rate to C/10. This action is labeled with "A" in Fig. 3e. With action "B", we set the current rate back to 2 C. For action "C", we disassembled the cell and added fresh electrolyte, and continued the cycling at current rate of 2 C. Finally, we set the current rate to C/10 as action "D".

Surprisingly, after action "A", the specific capacity recovered to 105 mAh/g, which is almost the same as a newly assembled one. Even after we set the current rate back to 2 C, the capacity recovered a lot compared to that before action "A". This means that in the 1400 times cycling at 2 C, the active material was rarely lost and nearly all of the capacity fading was caused by rising polarization, corresponding to the voltage profiles in Fig. 1b. The mechanical shaking wet the dried separator again with the conserved electrolyte inside the coin cell, which reduced the polarization but could not completely eliminate it. This residual polarization still existed even after we changed the cycled electrolyte with fresh electrolyte, which implies that the polarization was perhaps induced by SEI. Such analysis proved that our active materials are quite mature for industrial application, while the liquid electrolyte needs to be further optimized in the future.

3.3. Characterization of the poplar wood derived hard carbon and its half-cell performances

Woods are inherently porous at the xylem, and after carbonized at high temperatures, the porous structure remained as Fig. 4a shows. Without milling, a "honeycomb-like" morphology with a hole width of ~10 μm and a wall thickness of ~2 μm can be observed. This tends to give more uniform size of the milled particles.

The products exhibit different levels of graphitization at different pyrolysis temperatures, thus different morphologies, which is shown by TEM images in Fig. 4b and Supplementary Fig. S8-S10. While nano-graphite sections are rarely observed in Supplementary Fig. S8, more and more graphitic sections show up in Fig. 4a and Supplementary Fig. S9-S10 with increasing pyrolysis temperature. For PHC1600, as the TEM picture of Supplementary Fig. S10 shows, graphitic sections are evidently observed, which composed of 3 to 5 graphene layers.

The samples were characterized by XRD and Raman spectroscopy techniques. As displayed in Fig. 4c, XRD spectra reveal the amorphous character of samples by the presence of broad bands of both the two peaks of (0002) and (10$\bar{1}$0). With increasing pyrolysis temperature, the (0002) peak gradually shifts from 21.34° to 22.76°, and grows sharper, while the (10$\bar{1}$0) peak grows sharper too, but staying at 43.72°. The (0002) peak shift indicates that the *d*-spacing of the graphene layer decreased from about 0.416 nm to 0.390 nm, along with increasing graphitization levels [23]. The enhanced intensity of the (10$\bar{1}$0) peak along with growing pyrolysis temperature, reveals a more structured conjugated honeycomb lattice and thus less defects on the graphene fragments, which is consistent with the reported neutron scattering result [42]. As presented by Raman spectra in Fig. 4e, one can find G band at 1590 cm^{-1} corresponding to the only Raman active E_{2g} mode of the infinite graphite crystal [43], and conventionally named D band at 1342 cm^{-1} which was assigned to the A_{1g} mode activated for the small crystals of graphite, corresponding to the 'breathing mode' on the edge of the graphene layers, which could also be observed by grinding stress-annealed pyrolitic graphite [44,43]. Again, better short-range order could be confirmed by the sharper peaks at higher temperatures.

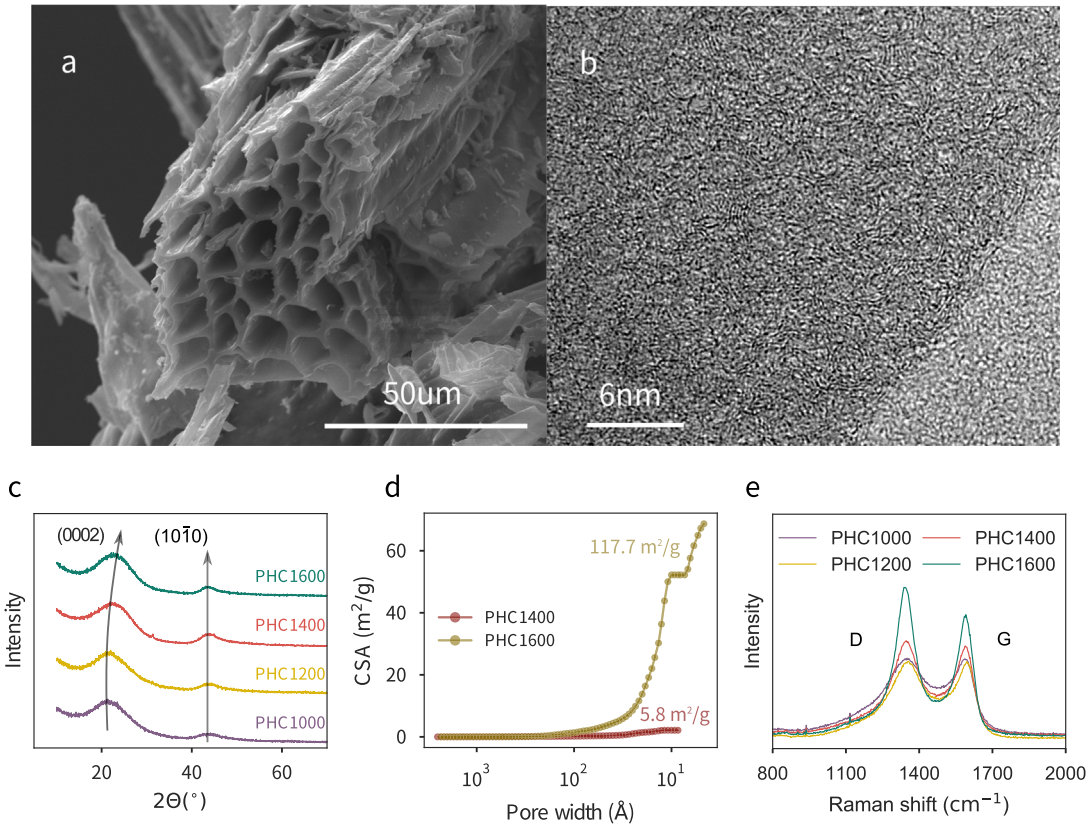

Fig. 4. Characterization of the PHC samples. (a) SEM pictures and (b) TEM pictures of PHC1400. (c) XRD patterns and (d) The Cumulative surface area(CSA) result of the N_2 adsorption/desorption experiment. (e) Raman spectra of PHC samples. The sample for SEM picture was without milling.

Discharge and charge profiles of the first two and the 100th cycles of the half-cells adopting hard carbon samples pyrolyzed at different temperatures are presented in Fig. 6a-d. Corresponding to the previous studies [45,46], the 'sloping' part of the profile declines and 'plateau' part of the profile increases with increasing carbonation temperature. And the potential of the plateau part tends to get lower with increasing temperature. The reversible specific capacities increase at first and then decrease with pyrolysis temperatures, reaching the maximum capacity of 330 mAh/g at 1400 °C. As presented in Fig. 6e, after cycling for 100 times at C/10, reversible specific capacities retain 89.0%, 94.5%, 97.0%, and 93.2% of the initial reversible specific capacities respectively. CV of the PHC samples is also provided as Supplementary Fig. S11.

For PHC1000, PHC1200, PHC1400 and PHC1600, ICEs were 84.6%, 85.6%, 88.3% and 87.0% respectively, and are higher than previously reported result [46,29,28,47]. ICE is normally believed to be sensitive to the surface area of the hard carbon, on which SEI forms, consuming the sodium ions from the cathode materials irreversibly. The Brunauer-Emmett-Teller (BET) surface area was usually provided as representative of the electrochemical active surface area. For PHC1400 (Supplementary Fig. S12), it was evaluated to about 5.8 m^2/g, but increased to be 117.7 m^2/g for PHC1600 (Supplementary Fig. S13). However, this ~20× increase of the BET surface area does not correspond to proportionally increasing ICI (=1-ICE). It was found that $ICI_{PHC1600}$ (13%) is only slightly higher than $ICI_{PHC1600}$ (11.7%), by 11%. We then carefully examined the pore size distribution through the cumulative surface area of the pores, and found that there are a huge number of pores around 1 nm for the PHC1600 samples, while nearly no pore on the surface of PHC1400 as shown in Fig. 4d. This could be an explanation for the slight increase of the ICI. Molecular dynamic simulation showed that the pores with a typical width around 1 nm could not hold the same environment to that of the bulk electrolyte [48]. The BET surface is not necessarily the electrochemical active surface (EAS) for SEI formation and can be much larger than EAS, as illustrated in Fig. 5. This might be because the electrolyte solvent molecule and the anion may need to change their coordination (which is difficult) to diffuse into and wet these 1 nm pores. This is a necessary condition for forming SEI, as electron needs to tunnel to the lowest energy unoccupied molecular orbital (LUMO) of the solvent or the anion, to initiate their reductive decomposition in order to form the SEI. The electron can only tunnel across a short distance, however, therefore wetting is a necessary condition.

Also, we could find in Fig. 5 that

$$\text{SEI weight gain}(n=1) \propto \sum_{\text{SEI}} A_{\text{SEIOS}} h_{\text{SEI}} \tag{14}$$

where A_{SEIOS} is the SEI outer surface area, and h_{SEI} is the average SEI height in that area. We note that typical SEI thickness on "outer" surfaces is on the order of 50 nm. Even in the first cycle, the thickness reaches 10 nm [49]. The inner surfaces with 1 nm open pores, even if they were accessible by electrolyte and electrically conductive (EAS), are so narrow that the SEI formed there (if it forms at all), will be very thin:

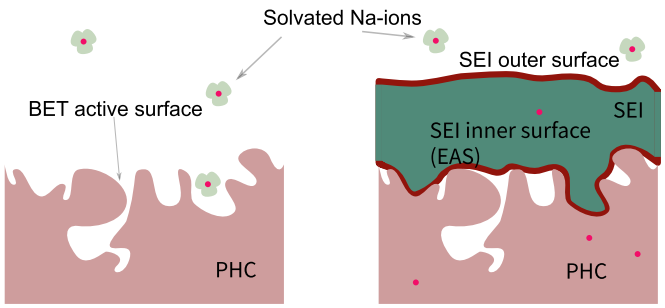

Fig. 5. SEI forming limited on the electrolyte accessible surface of the anode.

$$h_{SEI}(\text{inner surfaces}) \ll h_{SEI}(\text{outer surfaces}). \quad (15)$$

Thus, even though EAS has increased significantly, $\sum_{SEI} A_{SEIOS} h_{SEI}$ may not.

Poplar wood is plentiful all over the world, and is well known as a fast-growing tree species. The cost of Poplar wood is about 100 $ per ton and the yield is about 23.1% at the pyrolysis temperature of 1400 °C, resulting in a cost of ~430 $ ton^{-1} of the raw material. The low cost, high ICE, along with the high specific capacity of this anode material should give rise to more economical and higher performance SIB full-cells.

3.4. Half-cell performance vs. full-cell performance

We find that standard galvanostatic half-cell tests appear to give much poorer performance than full-cell tests, but later analysis shows this can be just an artifact of the half-cell measurement protocol (despite its popularity) and do not reflect intrinsic material performances. In half-cell tests, the results seem to show that hard carbon is usually marked with low rate performance, and we also get an enormous capacity fading under high rates as Fig. 6f presented. This conclusion turns out to be materially erroneous, due to the substantial voltage polarization at the Na metal counter-electrode.

The measured capacity of PHC1400 in standard half-cell tests with $[U_{min}, U_{max}]$ = [0V, 2.5V] is just about 180 mAh/g at 1C, corresponding to about 54.5% of the capacity at C/10. And for the 2 C condition, only about 22.7% of the capacity at C/10 remains. But for the full-cells (the same mass loading of ~2 mg/cm^2 PHC) as demonstrated in Table 1, 94.4% and 86.0% of the capacity at C/10 is retained at current rates of 1 C and 2 C respectively, and 73.5% even at a current rate of 5 C. So the sodium-matched NCNFM//PHC full-cell appears to have much better life and rate capability than PHC//Na half-cells. We will show below that this can be a measurement artifact.

Generally speaking, we can divide the PHC discharge profile into three parts. Part A entails rapidly changing $U_{PHC}(Q) > 0$ like in super-capacitor. Part B entails flattening $U_{PHC}(Q)$, but the open-circuit voltage (OCV) should still be positive $U_{PHC}^{OCV}(Q) > 0$ versus Na metal. Part B capacity contribution may associated with underpotential deposition (UPD) of sodium atoms. Both Part A and Part B should be highly reversible by definition and as our sodium-constrained full-cell tests have demonstrated. If we keep sodiating past the underpotential deposition limit, then we start to deposit genuine Na metal, which is Part C. Part C is not highly reversible - the Na metal will react strongly with liquid electrolyte, this will quickly dry out the electrolyte in full-cells. Thus, the real capacity of hard carbon could be defined as the capacity of Part A + Part B.

An *in situ* XRD experiment was performed to investigate the discharge profile of PHC with over-sodiation and to prove the new definition of the capacity, as Fig. 7a shows. A "V" cusp could be observed right before the Na peak showing up, which is caused by the energy barrier of nucleation of Na metal. This "V" cusp marks the transition from part B to part C, and could be regarded as the signature of the end of the highly reversible capacity. In this experiment conducted at C/30, the energy barrier of the nucleation of bulk Na

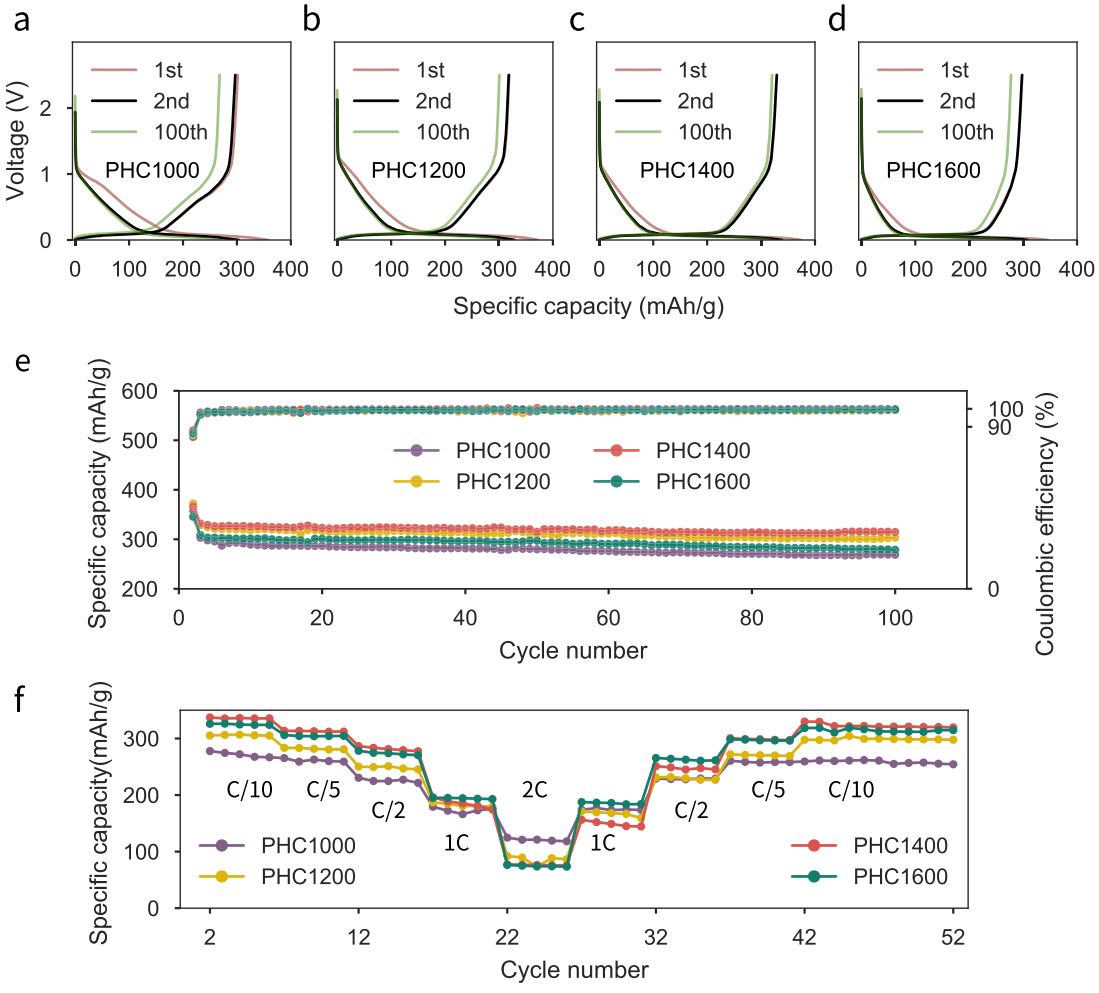

Fig. 6. Half-cell performance of the PHC samples. Charge/Discharge profiles of the half-cells of (a) PHC1000, (b) PHC1200, (c) PHC1400, (d) PHC1600. (e) The cycling performance and (f) the rate performance of the half-cells.

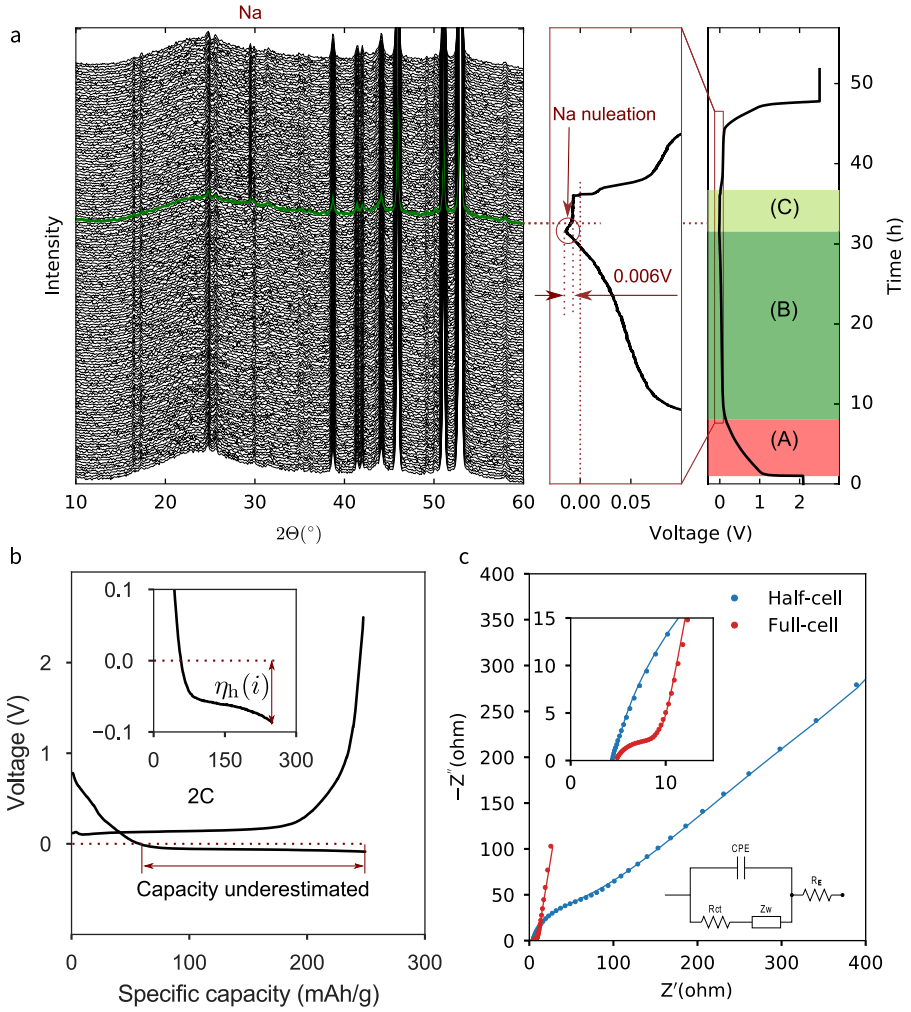

Fig. 7. The measurement problem of half-cells. (a) The*in situ* XRD spectra. The*in situ* XRD cell was cycled 2 times at C/10, then stabilized at 2.5 V for 12 h before the experiment. While the XRD spectra being collected, the cell was discharged at C/30 and then charged back to 2.5 V at C/10. (b) The capacity controlled cycling profile of the half-cell at 2 C. The discharge capacity was chosen to be 86.0%, which is the capacity reserving ratio of the full-cell at 2 C. The charging process was still cut off by voltage at 2.5 V. (c) The electrochemical impedance spectra of the newly assembled half-cell vs. full-cell indicates that the Na/electrolyte interface induces large impedance.

metal on PHC1400 is observed to be ~0.006 eV/atom. To compare this result with the high current rate deposition, a half-cell was discharged at 5C, and the energy barrier is approximately the same, as shown in Supplementary Fig. S14.

The problem in half-cell tests is associated with setting $U_{min} = 0$ V, which prematurely terminates Part B (even though it is still highly reversible), where U is the voltage between PHC electrode and metallic Na electrode. $U_{min} = 0$ V sounds like a very reasonable voltage cutoff in galvanostatic tests. But due to the impedance that is growing on the Na metal anode as well as the PHC electrode, there would be always $U_{min} = U^{OCV}_{PHC}(Q) - \eta(i) = 0$, and so $U^{OCV}_{PHC}(Q) > 0$ and we could still be in Part B. This turns out to lead to premature truncation of part of the PHC's real capacity.

To test this hypothesis, a capacity-controlled rather than voltage-controlled cycling of the half-cell at 2 C is performed and the result is presented as Fig. 7b. The discharge capacity is controlled to be 86.0% of the half-cell capacity at C/10, corresponding to the full-cell capacity reserving ratio at 2 C. The polarization at 2 C and the induced capacity underestimation is indicated in the figure. Without the "V" cusp appearing on the profile, the capacity corresponding to $U(Q) < 0$ V (but $U^{OCV}(Q) > 0$ V) could be charged back. As Supplementary Fig. S15 presents, the half-cell could be cycled at 2 C stably with a controlling discharge capacity of 86.0% of the capacity at C/10, and the average Coulombic efficiency is 99.8% through this cycling. This implies that the reversible rate capability of the hard carbon anode is actually much more optimistic than the half-cell rate capability presented in Fig. 6f with a rigid 0 V cutoff.

The full-cell test conducted with a similar rigid cut-off voltage (4.0 V at the end of sodiation of the hard carbon anode) surely suffers the same problem of premature truncation. Capacity of the full-cell is also underestimated and so as the rate capability. Supplementary Fig. S16 and Supplementary Fig. S17 demonstrate this effect. But the essential part is that the slopes at end of sodiation of hard carbon anode are different for the typical half-cell and full-cell, shown in the figures. The half-cell exhibits a voltage region quite low and near U_{min}, but this is not the condition for the full-cell near U_{max} (end of the sodiation of hard carbon). Thus, if they suffer the same polarization voltage loss, the capacity loss of half-cells would still be much more significant than the full-cells.

One may argue that the polarization of full-cells could be more significant than half-cells for the poor electron conductivity of NCNFM cathode. To check this, electrochemical impedance spectra (EIS) was taken for both a newly assembled half-cell and a newly assembled full-cell, presented as Fig. 7c. Note that without cycling (no SEI forming on the hard carbon anodes), the only difference of these two cells resides on the Na/NCNFM phases and their interfaces with the electrolyte, thus the half-cell should share the same equivalent circuit with the full-cell. Table S1 provides the fitting parameters of the EIS. R_E is the summation of Ohmic resistances of all the phases (including the Na/NCNFM phase, the hard carbon phase and the electrolyte phase) and

R_{ct} represents the Faradaic resistance for charge transferring through a specific interface. R_E of the full-cell is 4.9 Ω and is a little larger than that of the half-cell (4.6 Ω), which could be caused by the larger resistance of the NCNFM cathode material than Na metal, but the difference is small. However R_{ct} of the full-cell is much smaller than that of the half-cell. Because the interface between electrolyte and hard carbon is the same for the half-cell and full-cell, the R_{ct} difference is suspected to attribute to the interface between the electrolyte and Na/NCNFM. As presented in Table S1, the Na metal electrode induced a R_{ct} of 48.4 Ω, which is about 30× of the R_{ct} induced by the NCNFM electrode (1.6 Ω). Hence, the polarization of half-cells is actually much larger than that of the full-cell due to the Na metal SEI, which makes the underestimation of the half-cell capacity even worse.

We then traced the evolution of the EIS of the half-cell in cycling, and the result is presented in Supplementary Fig. S18. Compared to the initial state, which encounters no SEI on the hard carbon anode, there appears a new "semi-circle" at higher frequency, indicating the formation of SEI on hard carbon. The developing of the resistances are plotted in Supplementary Fig. S19. The Faradaic resistance of the SEI on hard carbon (R_1) is nearly constant, whereas the Faradaic resistance of the SEI on the Na metal electrode (R_2) increases with cycling, and becomes nearly constant after 5 cycles, corresponding to the Coulombic efficiency increasing in the first 5 cycles shown in Fig. 6e.

Thus, the rate performance of half-cell does not necessarily reflect the true rate capability of PHC. The capacity of the half-cell is more sensitive to polarization than that of the full-cell, and the impedance of the half-cell is larger than the full-cell due to instabilities on the Na metal electrode, which intensifies the effect of polarization. Hence, the rate capability of hard carbon should be preferably checked with full-cell testing. The same conclusion was drawn in another work [50].

4. Conclusions

In summary, we demonstrated a newly developed low-cost biomass hard carbon ($430/ton), delivering a high specific capacity of 330 mAh/g and an initial Coulombic efficiency of 88.3% in half cells. A SIB full-cell architecture with this hard carbon anode delivers a specific energy of 212.9 Wh/kg(AA+CA) at 1 C, with 71 % of the initial discharge capacity retained after 1200 cycles at 5 C. With an industrial-level mass loading (20.5 mg/cm^2 for the cathode), we get a capacity fade of only 6% within 600 cycles at 2 C, and the capacity could recover nearly completely by setting the current rate to C/10 after 1400 cycles, indicating the active electrode materials barely degraded. To our knowledge, this is the best full-cell SIB performance with hard carbon electrode.

The Coulombic inefficiency was carefully measured and analyzed. Coulombic inefficiency cumulant (CIC) analysis was performed to quantitatively check the industrial lore that "a Coulombic efficiency of 99.9% is required for a full-cell to cycle 200 times" due to $(0.999)^{200} = 0.8186$. However, significant Soluble Redox Mediator (SRM) effect was observed in this new sodium-ion full-cell, resulting in a much more optimistic cycle life than the CIC prediction, by a factor of 5. These SRMs do not cause significant self-discharge, either. We find that with static charge hold, SRM^{x-} was consumed mostly in day 1, followed by a linear self-discharging regime of −0.004 V/day, which is completely acceptable for most applications, even for grid-scale storage. The reason for this low self-discharge rate, despite the enhanced SRM^{x-}/SRM activity, is that the SRM^{x-} are generated only when the voltage is changing and the anode SEI is actively evolving, and could be consumed nearly completely in 1 day. In other words, during hold, the SRM^{x-} concentration (a function of both U and dU/dt, not just U) becomes very low after 3 days, and therefore the static-hold energy leakage rate is very low.

Furthermore, we demonstrated the difference in rate performance between half-cell and full-cell test protocols and proved that the same hard carbon would actually exhibit much more satisfactory rate performance in sodium-matched full-cell tests, due to a deficiency of the more commonly used half-cell testing protocol with a rigid 0 V cutoff. This work shows that although other components like the liquid electrolyte could be further optimized in the future, the cathode and anode materials are becoming mature and this is indeed an encouraging start for industrial-level SIBs.

Acknowledgements

This work was supported by funding from the National Key Technologies R & D Program, China (2016YFB0901500), NSFC (Grants no. 51725206, 51421002 and 51632001) and the One Hundred Talent Project of the Chinese Academy of Sciences. JL acknowledges ECCS-1610806.

Appendix A. Supplementary data

Supplementary data associated with this article can be found in the online version at http://dx.doi.org/10.1016/j.ensm.2018.09.002.

References

[1] D. Larcher, J.M. Tarascon, Nat. Chem. 7 (2015) 19–29.
[2] S. Shi, J. Gao, Y. Liu, Y. Zhao, Q. Wu, W. Ju, C. Ouyang, R. Xiao, Chin. Phys. B 25 (2016) 018212.
[3] S. Zhang, K. Zhao, T. Zhu, J. Li, Prog. Mater. Sci. 89 (2017) 479–521.
[4] Y. Jin, S. Li, A. Kushima, X. Zheng, Y. Sun, J. Xie, J. Sun, W. Xue, G. Zhou, J. Wu, F. Shi, R. Zhang, Z. Zhu, K. So, Y. Cui, J. Li, Energy Environ. Sci. 10 (2017) 580–592.
[5] T. Shiratsuchi, S. Okada, J. Yamaki, T. Nishida, J. Power Sources 159 (2006) 268–271.
[6] H. Liu, H. Zhou, L. Chen, Z. Tang, W. Yang, J. Power Sources 196 (2011) 814–819.
[7] D. Kim, S.H. Kang, M. Slater, S. Rood, J.T. Vaughey, N. Karan, M. Balasubramanian, C.S. Johnson, Adv. Energy Mater. 1 (2011) 333–336.
[8] R. Tripathi, G.R. Gardiner, M.S. Islam, L.F. Nazar, Chem. Mater. 23 (2011) 2278–2284.
[9] K. Chihara, A. Kitajou, I.D. Gocheva, S. Okada, J.-I Yamaki, J. Power Sources 227 (2013) 80–85.
[10] M.H. Han, E. Gonzalo, N. Sharma, J.M. López Del Amo, M. Armand, M. Avdeev, J.J. Saiz Garitaonandia, T. Rojo, Chem. Mater. 28 (2016) 106–116.
[11] Y. You, X. Yu, Y. Yin, K.W. Nam, Y.G. Guo, Nano Res. 8 (2014) 117–128.
[12] L. Mu, X. Qi, Y.S. Hu, H. Li, L. Chen, X. Huang, Energy Storage Sci. Technol. 5 (3) (2016) 324–328.
[13] X. Rong, J. Liu, E. Hu, Y. Liu, Y. Wang, J. Wu, X. Yu, K. Page, Y.-S. Hu, W. Yang, H. Li, X.-Q. Yang, L. Chen, X. Huang, Joule 2 (2018) 125–140.
[14] L. Li, Y. Xu, X. Sun, R. Chang, Y. Zhang, X. Zhang, J. Li, Adv. Energy Mater. 2 (2018) 1801064.
[15] P. Ge, M. Fouletier, Solid State Ion. 28–30 (1988) 1172–1175.
[16] M.D. Slater, D. Kim, E. Lee, C.S. Johnson, Adv. Funct. Mater. 23 (2013) 947–958.
[17] J. Qian, Y. Chen, L. Wu, Y. Cao, X. Ai, H. Yang, Chem. Commun. 48 (2012) 7070.
[18] L. Xiao, Y. Cao, J. Xiao, W. Wang, L. Kovarik, Z. Nie, J. Liu, Chem. Commun. 48 (2012) 3321.
[19] Y. Xu, Y. Zhu, Y. Liu, C. Wang, Adv. Energy Mater. 3 (2013) 128–133.
[20] Y. Li, Y. Lu, C. Zhao, Y.-S. Hu, M.-M. Titirici, H. Li, X. Huang, L. Chen, Energy Storage Mater. 7 (2017) 130–151.
[21] L. Zhao, J. Zhao, Y.-S. Hu, H. Li, Z. Zhou, M. Armand, L. Chen, Adv. Energy Mater. 2 (2012) 962–965.
[22] H. Zhao, J. Wang, Y. Zheng, J. Li, X. Han, G. He, Y. Du, Angew. Chemie - Int. 56 (2017) 15334–15338.
[23] R.E. Franklin, Acta Crystallogr. 4 (1951) 253–261.
[24] Y. Li, Y.S. Hu, X. Qi, X. Rong, H. Li, X. Huang, L. Chen, Energy Storage Mater. 5 (2016) 191–197.
[25] J.R. Dahn, W. Xing, Y. Gao, Carbon N.Y. 35 (1997) 825–830.
[26] E.M. Lotfabad, J. Ding, K. Cui, A. Kohandehghan, W.P. Kalisvaart, M. Hazelton, D. Mitlin, ACS Nano 8 (2014) 7115–7129.
[27] D. Zhou, M. Peer, Z. Yang, V.G. Pol, F.D. Key, J. Jorne, H.C. Foley, C.S. Johnson, J. Mater. Chem. A 4 (2016) 6271–6275.
[28] Y. Li, Y.-S. Hu, H. Li, L. Chen, X. Huang, J. Mater. Chem. A 4 (2016) 96–104.
[29] Y. Li, L. Mu, Y.S. Hu, H. Li, L. Chen, X. Huang, Energy Storage Mater. 2 (2016) 139–145.
[30] Q. Jiang, Z. Zhang, S. Yin, Z. Guo, S. Wang, C. Feng, Appl. Surf. Sci. 379 (2016) 73–82.
[31] Y. Li, Y.S. Hu, M.M. Titirici, L. Chen, X. Huang, Adv. Energy Mater. 6 (2016) 1600659.
[32] Z. Zhu, A. Kushima, Z. Yin, L. Qi, K. Amine, J. Lu, J. Li, Nat. Energy 1 (2016) 16111.
[33] Y. Li, Z. Wang, L. Li, S. Peng, L. Zhang, M. Srinivasan, S. Ramakrishna, Carbon N.Y. 99 (2016) 556–563.
[34] H.G. Wang, Z. Wu, F.L. Meng, D.L. Ma, X.L. Huang, L.M. Wang, X.B. Zhang,

ChemSusChem 6 (2013) 56–60.
[35] J. Zhang, Z. Zhang, X. Zhao, RSC Adv. 5 (2015) 104822–104828.
[36] C. Zhang, X. Wang, Q. Liang, X. Liu, Q. Weng, J. Liu, Y. Yang, Z. Dai, K. Ding, Y. Bando, J. Tang, D. Golberg, Nano Lett. 16 (2016) 2054–2060.
[37] J. Xu, M. Wang, N.P. Wickramaratne, M. Jaroniec, S. Dou, L. Dai, Adv. Mater. 27 (2015) 2042–2048.
[38] C. Zhao, Q. Wang, Y. Lu, B. Li, L. Chen, Y.-S. Hu, Sci. Bull. (2018). http://dx.doi.org/10.1016/j.scib.2018.07.018.
[39] G. Xu, J. Han, B. Ding, P. Nie, J. Pan, H. Dou, H. Li, X. Zhang, Green. Chem. 17 (2015) 1668–1674.
[40] Z. Wang, L. Qie, L. Yuan, W. Zhang, X. Hu, Y. Huang, Carbon N.Y. 55 (2013) 328–334.
[41] D. Li, H. Chen, G. Liu, M. Wei, L.X. Ding, S. Wang, H. Wang, Carbon N.Y. 94 (2015) 888–894.
[42] C. Bommier, T.W. Surta, M. Dolgos, X. Ji, Nano Lett. 15 (2015) 5888–5892.
[43] F. Tuinstra, J.L. Koenig, J. Chem. Phys. 53 (1970) 1126–1130.
[44] A.C. Ferrari, J.C. Meyer, V. Scardaci, C. Casiraghi, M. Lazzeri, F. Mauri, S. Piscanec, D. Jiang, K.S. Novoselov, S. Roth, A.K. Geim, Phys. Rev. Lett. 97 (2006) 1–4.
[45] S. Zhang, F. Yao, L. Yang, F. Zhang, S. Xu, Carbon N.Y. 93 (2015) 143–150.
[46] Y. Li, S. Xu, X. Wu, J. Yu, Y. Wang, Y.-S. Hu, H. Li, L. Chen, X. Huang, J. Mater. Chem. A 3 (2015) 71–77.
[47] N. Sun, H. Liu, B. Xu, J. Mater. Chem. A 3 (2015) 20560–20566.
[48] A. Karatrantos, Q. Cai, Phys. Chem. Chem. Phys. 18 (2016) 30761–30769.
[49] A. Kushima, K.P. So, C. Su, P. Bai, N. Kuriyama, T. Maebashi, Y. Fujiwara, M.Z. Bazant, J. Li, Nano Energy 32 (2017) 271–279.
[50] Y. Zheng, Y. Wang, Y. Lu, Y.-S. Hu, J. Li, Nano Energy 39 (2017) 489–498.